ISSN 1330-3651 (Print), ISSN 1848-6339 (Online) https://doi.org/10.17559/TV-20250228002428
Original scientific paper

# Time Series InSAR Monitoring and Analysis of Spatiotemporal Evolution Characteristics of Land deformation in Typical Artificial Islands around Hainan Island

Shusu DUAN*, Haixiang HUANG, Zhi ZHOU, XueXin YANG, Xin YANG, Weihua WANG, Xiaoxiang CHEN

**Abstract:** This study systematically investigated the spatiotemporal dynamics and underlying mechanisms of land deformation across three artificial islands in Hainan Province, China-Ocean Flower Island, Bright Pearl Island, and Wanning Sun Island, which adopts 29 Sentinel-1A ascending orbit SAR images acquired between May 2017 and June 2024. By integrating time series InSAR techniques (PS-InSAR and SBAS-InSAR) with leveling validation, we evaluated deformation trends and causative drivers through historical satellite imagery and sea level datasets to advance settlement monitoring methodologies. Key findings demonstrate the following relationships. (1) Strong agreement between PS-InSAR and SBAS-InSAR outputs in spatial deformation patterns and magnitudes, validating their utility for artificial islands stability assessment. (2) Distinct patterns of spatial and temporal evolution characterize settlement: rapid initial settlement during intensive construction phases (construction impact), followed by deceleration and eventual stabilization, with spatial hotspots localized in engineered zones. Anthropogenic activities amplify settlement rates compared to natural consolidation processes. (3) Differential marine hydrodynamics impacts are observed: Ocean Flower and Bright Pearl Islands display seaward-increasing settlement gradients correlated with wave energy distribution and seasonal sea level variations. In contrast, Wanning Sun Island's composite caisson-retaining wall system minimizes hydrodynamic disturbances, highlighting the role of structural engineering in mitigating marine hydrodynamics effects. The study establishes that artificial islands stability is governed by synergistic interactions among construction impact, coastal engineering design, and marine environmental forcing. These findings advance time series InSAR-based settlement monitoring frameworks and provide critical insights for optimizing disaster resilience in coastal reclamation projects, emphasizing the importance of integrating patterns of spatial and temporal evolution into urbanized island ecosystem management.

**Keywords:** artificial islands; construction impact; marine hydrodynamics; patterns of spatial and temporal evolution; Sentinel-1A; settlement monitoring; time series InSAR

## 1 INTRODUCTION

Hainan Island, located at the southernmost point of China, takes advantage of its unique features and strategic location. To expand development opportunities, improve competitiveness, and address the imbalance between land supply and demand, land reclamation and the creation of artificial islands have proven effective methods [1]. Currently, the monitoring of land levels and urban surface changes mainly depends on point-based geodetic techniques, such as precision leveling and global positioning systems (GPS). Although these traditional methods can deliver high-precision monitoring of surface changes at specific locations, they have several limitations, including a heavy workload, low efficiency, restricted spatial resolution, and high costs [2]. Additionally, these techniques only provide information on settlement at individual points, making it challenging to capture the overall trend and exact extent of land deformation. In contrast, interferometric methods utilizing synthetic aperture radar (InSAR) data present several benefits, such as extensive spatial coverage, high spatial resolution, operation in all weather conditions, and accurate deformation measurement [3-5]. However, conventional InSAR methods encounter issues like temporal and spatial decorrelation, as well as atmospheric delays. To overcome these challenges, techniques such as permanent scatterer (PS) and small baseline subset (SBAS) time-series analysis have been developed [6- 8]. These methods are now widely adopted for monitoring surface deformation, detecting landslides, and seismic monitoring, and are regarded as crucial tools in these fields [9].

Research on land settlement in reclamation areas has gained attention due to its intricate causes and the associated environmental and engineering risks. Various studies have utilized different InSAR techniques to investigate land settlement in these zones, uncovering both spatial and temporal settlement patterns and identifying significant influencing factors. For instance, Cavalié analyzed 47 ascending and 40 descending ENVISAT ASAR images with NSBAS technology to track land settlement at Nice Côte d'Azur Airport in France, finding a maximum cumulative settlement of 72 mm over eight years from 2003 to 2011. The settlement rate was initially rapid during the early reclamation phase before stabilizing, with the majority of settlements occurring in the reclaimed area, influenced by the oceanic dynamic environment and geological structure [10]. Similarly, Li-Ming Jiang conducted a long-term study at Hong Kong Chek Lap Kok Airport using the IPTA method and 25 ENVISAT ASAR scenes, which revealed a maximum cumulative settlement of 100 mm from 2003 to 2008. A settlement trend was noted across most of the reclaimed area, with an initially high rate that gradually stabilized, influenced by the characteristics of reclamation materials and ground water level variations, particularly in the north and south runways and midfield development area, especially in regions with poor geological conditions [11]. Additionally, Min Zeng employed a 24-image Sentinel-1A dataset with the PS-InSAR method to monitor land deformation in a typical reclaimed area of the Pearl River Estuary, finding a maximum cumulative settlement of 117 mm between 2015 and 2016. The settlement occurred rapidly in the short term before stabilizing, primarily in areas with thick soft soil and high human activity, which were identified as key factors contributing to uneven settlement [12]. Lastly, Nie Yunju used 22 Sentinel-1A images and SBAS-InSAR to monitor settlement in the Shenzhen reclamation area, reporting a maximum cumulative settlement of 50 mm from 2020 to 2021, with an intensified settlement rate towards the end of the study. The settlement was mainly concentrated in the eastern part of the reclaimed area, showing an increasing trend from west to east, influenced by the water table and construction activities [13].

The aforementioned studies indicate that earlier research has recognized land settlement in artificial islands at airports and urban reclamation sites, and has thoroughly examined its spatial and temporal changes. In terms of

time, settlement rates are generally quicker during the early phases of reclamation, followed by a gradual stabilization. Spatially, settlement tends to occur mainly in areas with softer reclamation materials or where construction activities are more prevalent. These results suggest that land settlement in reclaimed regions is affected by various factors, including the characteristics of reclamation materials, the construction process, fluctuations in the water table, consolidation of soft soils, and human activities. However, there is still insufficient research on land settlement in artificial islands in the South China Sea, especially in Hainan, where the unique tropical monsoon climate and complex marine environment pose significant challenges to the stability of these islands. The intricate water environment around Hainan's artificial islands, along with the limited time for consolidation and settlement, poses challenges to achieving a stable deformation state. Consequently, both overall and differential settlement are likely to occur over the long-term use of these islands [14, 15]. Additionally, the settlement process is affected by multiple factors, and the spatial and temporal evolution of land deformation has not been thoroughly investigated. The tropical monsoon climate of Hainan Island, characterized by high humidity, heat, salt spray, and intense radiation, further complicates the settlement issue due to the specific construction materials used in this environment. Therefore, it is essential to monitor settlement on artificial islands around Hainan to ensure infrastructure safety and stability and to mitigate potential hazards.

This study focuses on Ocean Flower Island, Bright Pearl Island, and Wanning Sun Island, utilizing 29 Sentinel-1A image scenes from May 2017 to June 2024. SBAS-InSAR and PS-InSAR techniques are employed to validate leveling measurement data and calibrate experimental parameters for Ocean Flower Island. The analysis includes annual mean settlement rates and their variations at identical latitude and longitude points through correlation studies and normal distribution fittings, ensuring consistency between the results of the two methods and enhancing the reliability and accuracy of settlement monitoring in the study areas. Furthermore, the spatial and temporal patterns of land settlement on artificial islands in Hainan Province, along with their underlying causes, are explored to aid in the monitoring of offshore artificial islands in China and to contribute to the prevention and management of geological hazards in artificial island reclamation projects and related research.

## 2 MATERIALS AND METHODS

### 2.1 Study Area

Ocean Flower Island, a significant geographical feature in Danzhou City, Hainan Province, China, is situated in the shallow bay between Paipu Harbor and Yangpu Harbor, with coordinates 19°39'51"N, 109°10'27"E. The island covers approximately 7.8 square kilometers and is designed to accommodate around 115,800 residents. As depicted in Fig. 1a, it comprises three sub-islands (Island 1#, Island 2#, and Island 3#). Island 1# is further divided into six sections, labeled A to F, which are linked to the main land through dykes and box culverts, creating a distinctive system of internal and external marine waters [16]. The full reclamation of Ocean Flower Island was completed in March 2017, with areas A, C, D, E, and F of Island 1# finished by December 2015.

The South China Sea Pearl Artificial Island, also referred to as Bright Pearl Island, is located in the south eastern region of the Beibu Gulf in the South China Sea, with central coordinates of 18°30'00"N, 111°20'00"E. The island has a planned area of 4.6 square kilometers and features a circular enclosed area with a shoreline of approximately 7.7 kilometers. As shown in Fig. 1b, the southern part of the enclosed area includes a road, while the northern section contains water, with 2.56 square kilometers of land [17]. The island is situated about 1.8 km from the west coast of Haikou, connected by the South China Sea Pearl Bridge. Its reclamation was also completed in March 2017.

Wanning Sun Island is located in Wanning City, Hainan Province, positioned between the Gaxin and Tianxin administrative districts and bordered to the west by Niuling County. The reclaimed sea area is approximately 0.48 square kilometers, with a total planned area of 0.6 square kilometers, of which 0.5 square kilometers is intended for construction and 0.1 square kilometers for non-construction purposes. The reclamation of this island was finalized in February 2013 [18], as illustrated in Fig. 1c.

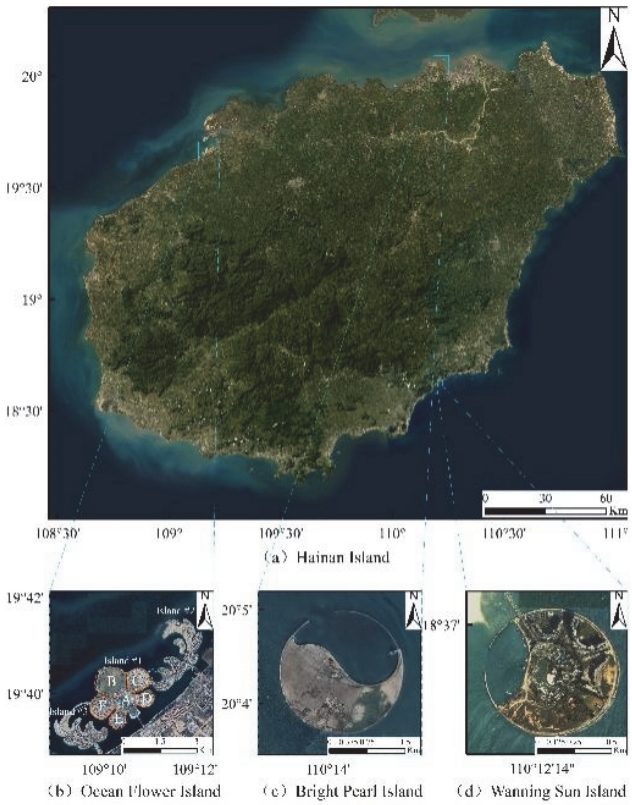


**Figure 1** Location of the study area

### 2.2 Data

This research employs Sentinel-1A image data to track the land deformation patterns of Ocean Flower Island, Bright Pearl Island, and Wanning Sun Island in Hainan Province, while also analyzing the spatial and temporal changes in settlement in these regions. A selection of 29 ascending single-view complex images from Sentinel-1A, featuring VV polarization and a resolution of 5 × 20 m, was

made, covering the time frame from May 21, 2017, to June 24, 2024. Orbital calibration was conducted using the POD precision orbiting ephemeris data, and terrain phase errors were corrected with 30 m resolution ASTER GDEM V3 data. Time-series InSAR technology was applied for monitoring land deformation, and the spatial data management and analysis capabilities of GIS were utilized to thoroughly investigate the spatial and temporal settlement patterns [19]. The key parameters for the study are listed in Tab. 1. The Sentinel-1A data were processed using ENVI software, and the findings, along with additional data, were imported into ArcGIS software for comprehensive analysis and mapping. Monthly sea level height data from 2017 to 2023, obtained from the China Ocean Information Network (COIN), were used to assess the impact of sea level height on surface deformation (refer to Tab. 2 and Tab. 3).

**Table 1** Sentinel-1A image data parameters

| Date | Parameter | description |
|---|---|---|
| Sentinel-1A | Data pattern | Interference width |
| | Time range | 2017-05-21 - 2024-06-24 |
| | Data volume/scene | 29 |
| | Orbital direction | Ascending |
| | Width/km | 250 |
| | Spatial resolution / $m^2$ | 5 × 20 |
| | Revisit period / d | 12 |
| | Incidence angle / ° | 37 |
| | Polarization mode | VV |
| | Radar wave length / cm | 5.6 |
| ASTER GDEM V3 | Spatial resolution / m | 30 |
| Google Earth | Spatial resolution / m | 0.465 |

**Table 2** Sea surface height data in the eastern part of Hainan Island from 2017 to 2023

| Year | Jan | Feb | Mar | Apr | May | June | July | Aug | Sep | Oct | Now | Dec |
|---|---|---|---|---|---|---|---|---|---|---|---|---|
| 2017 | 180 | 130 | 110 | 50 | 0 | −80 | 10 | −10 | 130 | 400 | 230 | 150 |
| 2018 | 80 | 0 | −40 | −30 | −70 | 0 | 30 | 50 | 100 | 220 | 180 | 170 |
| 2019 | 110 | 20 | 30 | 20 | 70 | −50 | −60 | −10 | 180 | 200 | 230 | 120 |
| 2020 | 10 | 10 | −40 | 0 | −100 | −120 | −140 | −40 | 80 | 480 | 250 | 200 |
| 2021 | 60 | 0 | 10 | 90 | −50 | −90 | 0 | −60 | 10 | 300 | 170 | 200 |
| 2022 | 100 | 120 | 0 | 30 | 40 | −80 | 0 | 20 | 160 | 360 | 180 | 200 |
| 2023 | 80 | 80 | −40 | −20 | 30 | −30 | −20 | −30 | 150 | 250 | 190 | 120 |

**Table 3** Sea surface height data in the western part of Hainan Island from 2017 to 2023

| Year | Jan | Feb | Mar | Apr | May | June | July | Aug | Sep | Oct | Now | Dec |
|---|---|---|---|---|---|---|---|---|---|---|---|---|
| 2017 | 180 | 130 | 140 | 100 | 50 | 40 | 60 | 50 | 170 | 360 | 230 | 170 |
| 2018 | 100 | 10 | 20 | 30 | 40 | 20 | 30 | 10 | 60 | 390 | 180 | 130 |
| 2019 | 110 | 50 | 60 | 80 | 90 | 0 | −40 | −20 | 80 | 150 | 230 | 70 |
| 2020 | 50 | 40 | 0 | 10 | −20 | −10 | −20 | 10 | 90 | 390 | 220 | 130 |
| 2021 | 20 | −10 | 40 | 110 | 20 | −40 | 10 | −20 | 40 | 200 | 140 | 100 |
| 2022 | 100 | 90 | 20 | 40 | 50 | −10 | 20 | 30 | 150 | 270 | 180 | 170 |
| 2023 | 30 | 90 | 0 | 40 | 60 | 20 | 0 | −10 | 110 | 170 | 140 | 120 |

### 2.3 Ocean Flower Island Levelling

Level measurements on Ocean Flower Island in the sea began at the end of 2015, resulting in a total of 15 data points collected over various time periods. Island 3# is designated from L1 to L5, Island 1# from L6 to L10, and Island 2# from L11 to L15, with observations conducted monthly. As per the Specification for Measurement of Water Transportation Projects (JTS131-2012), the seawall monitoring level is categorized as fourth class, and the deformation observation points have an accuracy of ±12.0 mm for horizontal positioning and ±4.0 mm for elevation, in relation to the nearest datum.

**Table 4** Leveling benchmark coordinates on Ocean Flower Island

| Point | *X* | *Y* |
|---|---|---|
| L1 | 173721.854 | 73172.824 |
| L2 | 173885.258 | 72881.945 |
| L3 | 173877.412 | 72396.367 |
| L4 | 174165.263 | 72224.424 |
| L5 | 174643.425 | 72076.841 |
| L6 | 174780.239 | 74022407 |
| L7 | 176721.730 | 73753.485 |
| L8 | 176150.378 | 74642.181 |
| L9 | 175829.650 | 75313.276 |
| L10 | 175334.144 | 75105.001 |
| L11 | 176197.069 | 75816.694 |
| L12 | 176939.442 | 76363.474 |
| L13 | 178138.902 | 76536.665 |
| L14 | 178451.997 | 76846.892 |
| L15 | 178221.691 | 75944.274 |

The leveling measurements in this research are based on the 1985 national elevation datum. Detailed coordinates can be found in Tab. 4, and the layout of the leveling points is depicted in Fig. 2.

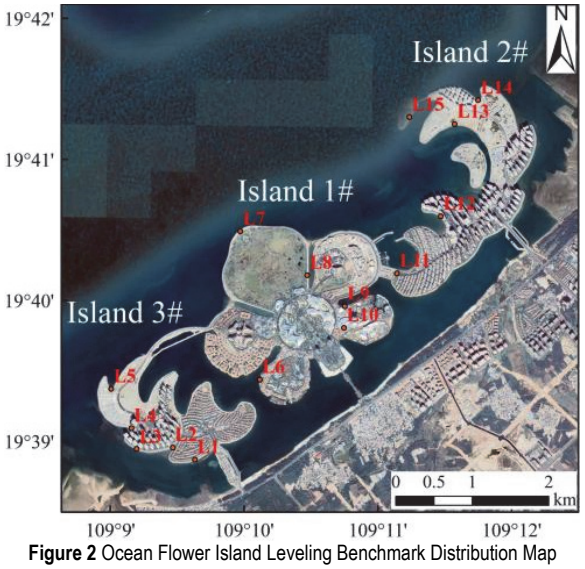


**Figure 2** Ocean Flower Island Leveling Benchmark Distribution Map

### 2.3 Method

#### 2.3.1 PS-InSAR Processing

The PS-InSAR processing sequence is outlined with the following detailed steps and key parameters:

1. Creation of connectivity maps: Connectivity maps for Ocean Flower Island, Bright Pearl Island, and Wanning Sun Island are produced, using the image from February 17, 2021, as the reference for all three islands.

2. Interference processing: The quality of the Digital Elevation Model (DEM) affects the accuracy of leveling corrections. To address this, processed ASTER GDEM V3 data for the Hainan Island area are utilized to eliminate phase errors resulting from leveling.

3. Selection of PS points: A coherence coefficient threshold of 0.70 and an amplitude deviation threshold of 0.3 are established.

4. PS inversion: A linear model is employed to estimate residual topography and deformation rates. The spatial distribution of atmospheric variations is set to 1000m, while the temporal distribution spans 450 days, with nonlinear deformation phases being distinguished.

5. Geocoding: The vertical mean annual deformation rate for the study area is obtained through geocoding, and temporal and spatial analyses are performed using ArcGIS.

### 2.3.2 SABS-InSAR Processing

The SBAS-InSAR processing workflow is illustrated with the following detailed steps and important parameters:

1. **Connection Graph**: Utilizing 29 views of SAR image data along with a common master image, the critical baseline percentage is capped at 45%, and the maximum spatial baseline is set to 500m. This results in the creation of 106 interferometric pairs for Ocean Flower Island, Bright Pearl Island, and Wanning Sun Island.

2. **Interferometric Process**: The Goldstein filtering method is employed to minimize noise in the interferogram and improve the signal-to-noise ratio. The Delaunay MCF technique is applied for phase unwrapping, with a coherence coefficient threshold established at 0.25. Interferometric pairs that exhibit low coherence or inadequate unwrapping outcomes are discarded.

3. **Refinement and Re-Flattening**: The remaining constant phase and phase ramp errors after unwrapping are assessed and eliminated. Ground control points (GCPs) are identified, and the processing of these points is fine-tuned until the residuals are minimized. The flat earth effect is corrected using a polynomial approach to address track parameter inaccuracies.

4. **SBAS Inversion**: A linear model is initially utilized to estimate the deformation rate and terrain error. Atmospheric delay errors are subsequently corrected through high-pass filtering in the time domain and low-pass filtering in the spatial domain.

5. **Geocoding**: The vertical mean annual deformation rate for the area under study is obtained through geocoding, and both temporal and spatial analyses are performed using ArcGIS.

## 3 RESULTS

### 3.1 Surface Deformation Monitoring Results

#### 3.1.1 Results of Surface Deformation Monitoring based on PS-InSAR Technology

Fig. 3 illustrates the distribution of surface deformation rates in the study area from May 2017 to June 2024, obtained through the PS-InSAR technique. For Ocean Flower Island, the vertical surface deformation rates range from –15.94 to 5.02 mm/a, while Bright Pearl Island shows rates from –11.05 to 4.86 mm/a, and Wanning Sun Island has rates between –6.92 to 3.89 mm/a.

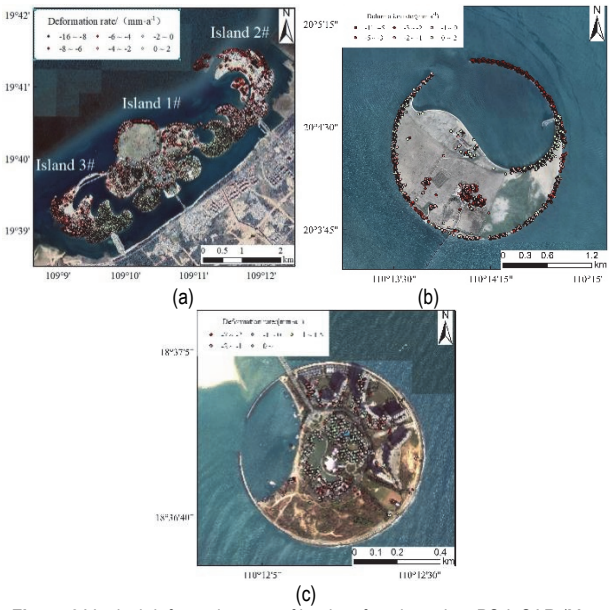


**Figure 3** Vertical deformation rate of land surface based on PS-InSAR (May 2017 to June 2024). (a) Ocean Flower Island; (b) Bright Pearl Island; (c) Wanning Sun Island

As depicted in Fig. 3a, Ocean Flower Island mainly undergoes surface settlement, with some uplift observed only in the inner sea area. The outer sea regions of Ocean Flower Island have a higher concentration of severe settlement points, indicating that settlement is the primary form of deformation. The inner sea area has a few uplift points. In the B area of Island 1#, as well as Islands 2# and 3#, the presence of vegetation and sandy land has led to a loss of coherence, resulting in fewer detectable deformation points. The surface settlement rates on Ocean Flower Island are primarily between –4.56 to 1.52 mm/a, with an average annual settlement rate of –1.35 mm/a, and some areas experiencing rates as high as –15.94 mm/a.

Fig. 3b indicates that Bright Pearl Island's surface deformation is largely characterized by settlement, with only a few isolated uplift areas. The deformation points are more densely located along the island's outer coastline, while the inner region has fewer points due to vegetation and sandy surfaces that lack stable reflectors, significantly reducing the number of detectable deformation points. The surface settlement rates on Bright Pearl Island generally range from –3.29 to 1.14 mm/a, with an average annual settlement rate of –1.47 mm/a, and some areas experiencing rates up to –11.05 mm/a.

According to Fig. 3c, Wanning Sun Island shows relatively stable settlement, with the most significant deformation occurring along the island's outer ring. Only a few scattered uplift areas are found within the inner ring. The number of surface deformation points in the inner region is notably lower due to the absence of stable reflectors on the vegetated and sandy surfaces. The surface settlement rates across the island mainly range from –2.34 to 1.58 mm/a, with an average annual settlement rate of –0.49 mm/a, and certain areas experiencing rates as high as –6.92 mm/a.

### 3.1.2 Results of Surface Deformation Monitoring Based on SBAS-InSAR Technology

Fig. 4 displays the distribution of surface deformation rates in the study area from May 2017 to June 2024, obtained through the SBAS-InSAR technique. The vertical surface deformation rates vary from –13.09 to 2.11 mm/a for Ocean Flower Island, –8.22 to 2.16 mm/a for Bright Pearl Island, and –3.48 to 1.74 mm/a for Wanning Sun Island.

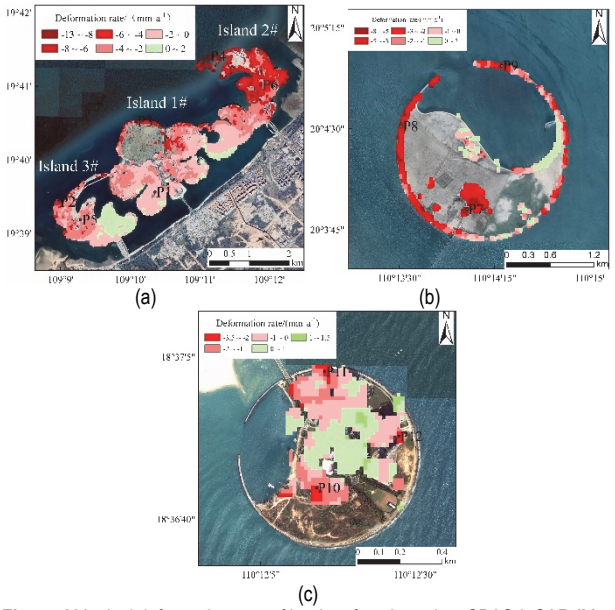


**Figure 4** Vertical deformation rate of land surface based on SBAS-InSAR (May 2017 to June 2024). (a) Ocean Flower Island; (b) Bright Pearl Island; (c) Wanning Sun Island

As depicted in Fig. 4a, the surface settlement points on Ocean Flower Island are more dispersed, with some regions in the inner sea showing occasional uplift. The loss of coherence in certain areas of the islands, due to vegetation and sandy terrain, has led to a reduced number of detectable deformation points. The outer coast of Ocean Flower Island and the upper section of Island 2# mainly show surface settlement points, with settlement becoming more pronounced closer to the outer coast. Conversely, the inner sea area has a more uniform distribution of surface settlement and uplift points, with uplift points being more prevalent. The overall surface settlement rates for Ocean Flower Island are primarily between –4.24 and 0.59 mm/a, with an average annual settlement rate of –1.95 mm/a, and some areas experiencing rates as low as –13.09 mm/a.

Fig. 4b indicates that there are more surface settlement points along the outer coast of Bright Pearl Island, while uplift is only observed in sporadic areas within the inner region. The northern and western parts of Bright Pearl Island have a higher concentration of settlement deformation points, predominantly characterized by surface settlement. In the inner sea area, building deformation points are evenly distributed, but fewer points are found in sandy soil and vegetation-covered regions. The surface settlement rates on Bright Pearl Island mainly range from –4.69 to 0.08 mm/a, with an average settlement rate of –2.09 mm/a in some areas, and reaching as high as –8.22 mm/a in others.

According to Fig. 4c, Wanning Sun Island experiences relatively mild settlement, with the most significant deformation occurring along the outer edge of the island, particularly in buildings. Only a few isolated areas in the interior show uplift. There are fewer deformation points in regions with sandy soil and vegetation. The surface settlement rates across Wanning Sun Island generally range from –1.86 to 1.29 mm/a, with an average annual settlement rate of –0.41 mm/a, and some areas experiencing rates up to –3.48 mm/a.

## 3.2 Accuracy Verification

### 3.2.1 Internal Conformity Accuracy Verification

Numerical statistics of the standard deviation of the vertical average deformation rate from PS-InSAR were carried out for Ocean Flower Island, Bright Pearl Island, and Wanning Sun Island, resulting in probability density function curves of the standard deviation of the deformation rate (Fig. 5).

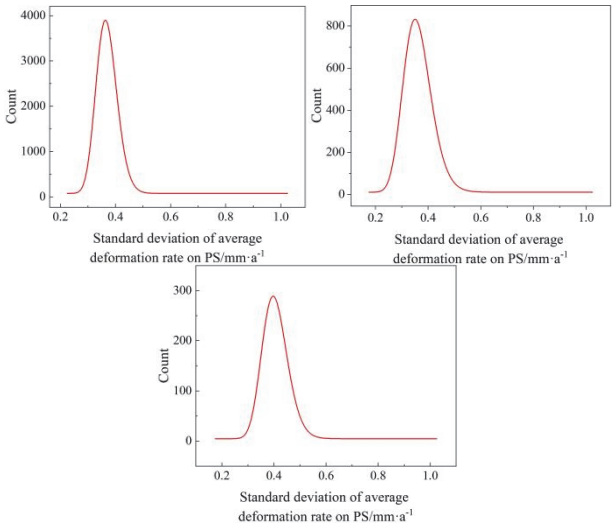


**Figure 5** Probability density function of the standard deviation of mean deformation rate on PS. (a) Ocean Flower Island; (b) Bright Pearl Island; (c) Wanning Sun Island

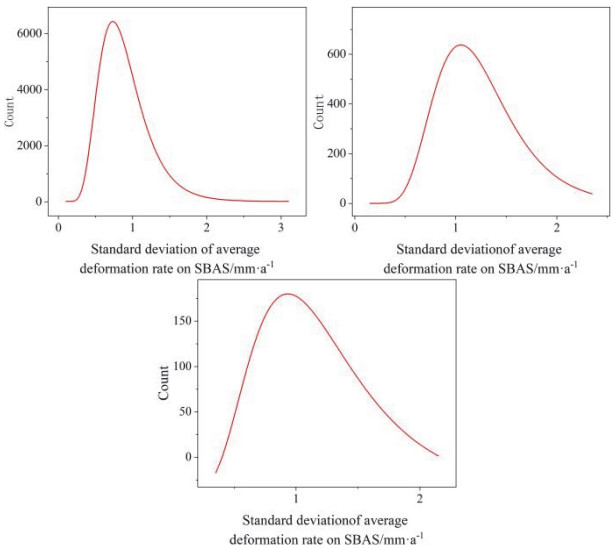


**Figure 6** Probability density function of the standard deviation of mean deformation rate on SBAS: (a) Ocean Flower Island; (b) Bright Pearl Island; (c) Wanning Sun Island

The standard deviations of the target points are all below 2 mm/a. These results meet the criteria in the "Geological Hazard InSAR Monitoring Technical Guidelines", and the internal accuracy of PS-InSAR should be less than 2 mm/a. Subsequently, numerical statistics of the standard deviation of the vertical average deformation rate from SBAS-InSAR were carried out for Haikou Flower Island, Bright Pearl Island, and Wanning Sun Island, resulting in probability density function curves of the standard deviation of the deformation rate (Fig. 6). The standard deviations of the target points for Haikou Flower Island, Bright Pearl Island, and Wanning Sun Island are all below 5 mm/a. These results meet the criteria in the "Geological Hazard InSAR Monitoring Technical Guidelines" that the internal accuracy of SBAS-InSAR should be less than 5 mm/a. This indicates that the ground monitoring results are highly precise and accurate.

### 3.2.2 External Conformity Accuracy Verification

The leveling benchmarks on Ocean Flower Island (L1-L15, Fig. 2) are strategically distributed to cover core settlement-sensitive zones, including construction-intensive areas (e.g., Blocks A–F of Island 1#), reclamation boundaries (e.g., L1-L5 on Island 3#), and coastal dynamic regions (e.g., L13-L15 on Island 2#). The placement complies with the fourth-class monitoring standards of the Specification for Measurement of Water Transportation Projects (JTS131-2012), ensuring spatial representativeness and engineering safety.

The leveling data and InSAR observation results were organized within the same spatial and temporal reference frame, with specific coordinates provided in Tab. 4. The comparison results are shown in Fig. 7, which indicate a good consistency between InSAR and leveling measurements.

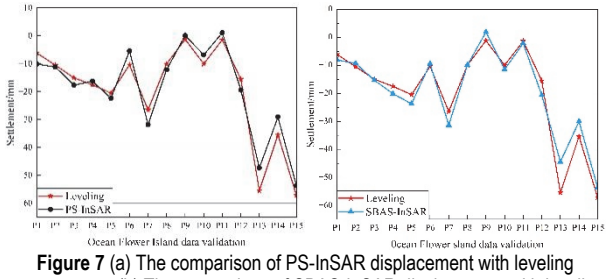


**Figure 7** (a) The comparison of PS-InSAR displacement with leveling measurement (b) The comparison of SBAS-InSAR displacement with leveling measurement

Displacement measurements from individual interferograms are often influenced by artifacts due to atmospheric delays and variations in satellite orbits and terrain data, which can lower InSAR accuracy [20]. Differences of up to 10 mm were observed at some leveling points, which can be attributed to two main factors. First, InSAR measurements reflect annual mean rates from multiple interferograms, whereas leveling measurements capture time-varying displacements, leading to differences between both. Second, larger differences were noted in areas with steeper deformation gradients. For instance, leveling points L13, L14, and L15 (Fig. 7) are located offshore of Island 2, where settlement is more pronounced. However, compared to other areas, fewer inversion points are identified near these leveling points. This, combined with the large deformation gradient and the limited spatial resolution of the inversion points, also contributes to the observed bias. The standard deviations for Fig. 7a, and Fig. 7b are 1.48 mm and 1.41 mm, respectively.

Due to the absence of leveling measurement data for Bright Pearl Island and Wanning Sun Island, we performed normal distribution fitting and difference correlation analysis on 1,768 and 169 feature points, which extracted by PS-InSAR and SBAS-InSAR methods for Bright Pearl Island and Wanning Sun Island, respectively, as shown in Fig. 8.

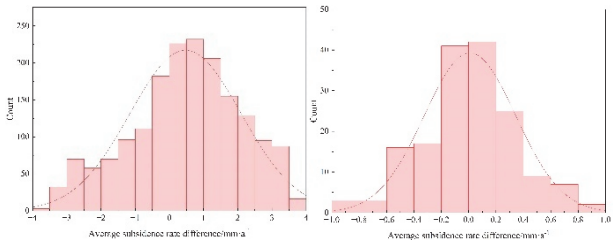


**Figure 8** Distribution of annual average settlement rate difference between the two methods (a) Bright Pearl Island (b) Wanning Sun Island

For Bright Pearl Island, the mean and standard deviation of the differences in annual average settlement rates between the two methods is 0.47 mm/a and 1.62 mm/a, respectively. For Wanning Sun Island, the corresponding values are –0.02 mm/a and 0.40 mm/a. The difference correlation analysis is presented in Fig. 9, with R-squared values of 0.7542 and 0.8948, and root-mean-square errors of 0.63 mm/a and 0.15 mm/a for Bright Pearl Island and Wanning Sun Island, respectively. Both results meet the accuracy requirements of CH/T6006-2018 "Specifications for Processing Time-Series InSAR Surface Deformation Monitoring Data," indicating that the results of the two methods are highly consistent and comply with relevant technical specifications, reflecting a relatively low and stable settlement risk in the study area. Given the advantages of SBAS-InSAR in terms of data processing efficiency and coverage, the subsequent analysis will be based on the SBAS-InSAR results for presentation and discussion.

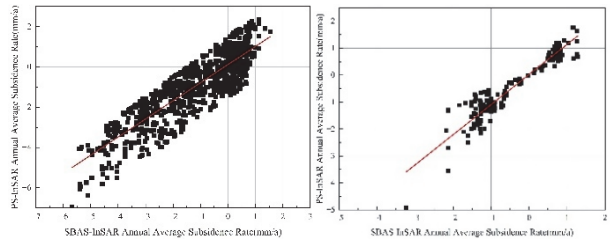


**Figure 9** Comparison and validation of monitoring results between PS-InSAR and SBAS-InSAR(a) Bright Pearl Island(b) Wanning Sun Island

## 4 DISCUSSION

### 4.1 Spatial and Temporal Variations in Land Deformation on Artificial Islands

To investigate the spatial evolution of land deformation on the artificial islands, the cumulative deformation data for Ocean Flower Island, Bright Pearl Island, and Wanning Sun Island from May 2017 to June 2024 were shown in Fig. 10 to Fig. 12, which explore the

spatial evolution patterns of land deformation on the artificial islands. As depicted in Fig. 10, from 2017 to 2024, the outer sea area of Ocean Flower Island experienced a more significant growth in settlement, while the inner sea area remained relatively stable overall. The cumulative settlement in most regions ranged from –30 mm to 10 mm. Notably, continuous settlement was observed along the outer sea and in the construction areas of Islands 2# and 3#, where these areas exhibited an expanding settlement zone, maintained a relatively high settlement rate, and experienced a fluctuating upward trend in cumulative settlement. Between May 2017 and August 2017, sporadic settlement occurred across the entire island, with some areas exhibiting uplift. From August 2017 to February 2019, as construction progressed, the settlement began in the central region of Ocean Flower Island, gradually extending outward to surrounding areas and the coastline. The maximum cumulative settlement during this period reached 49.53 mm. From February 2019 to August 2021, settlement continued, and between August 2021 and February 2022, the settlement area expanded across the island due to increased human activity. This led to a significant rise in ground load, intensifying settlement, with the maximum settlement reaching 67.83 mm. From February 2022 to June 2024, the overall settlement began to stabilize, with the settlement rate gradually slowing; nevertheless, the cumulative settlement continued to increase, with the area near the outer sea of Island 2# experiencing the most severe settlement, reaching a maximum cumulative settlement of 88.01 mm.

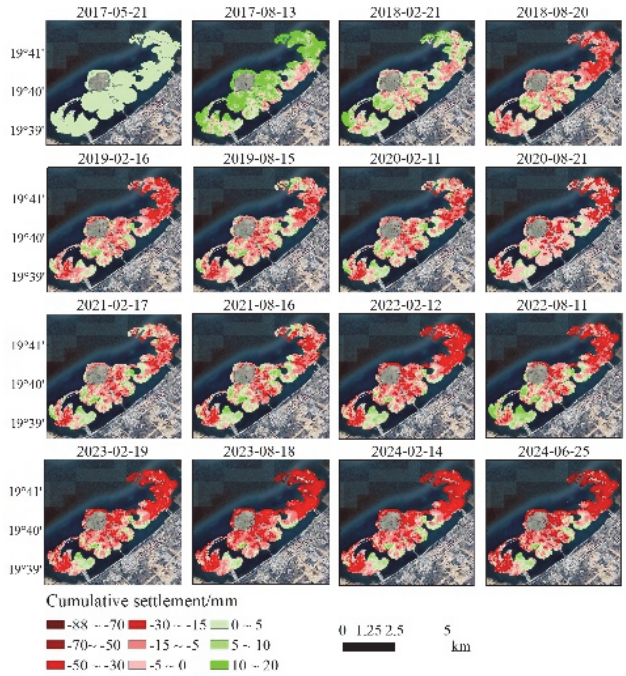


**Figure 10** Time-series cumulative surface settlement in Ocean Flower Island

As seen in Fig. 11, during the monitoring period from 2017 to 2024, settlement in certain areas of Bright Pearl Island showed a slight increase, though overall, the island remained fairly stable, with most regions experiencing cumulative settlement between –25 mm and 5 mm. Notably, rapid and ongoing settlement was observed in the building areas, along the northern and western sides near the outer sea, with the settlement area on Bright Pearl Island expanding, resulting in an upward trend in cumulative settlement. From May 2017 to February 2018, cumulative settlement on the island increased quickly, reaching a maximum of 21.3 mm. From February 2018 to August 2020, the settlement area further expanded, with the maximum cumulative settlement rising to 41.2 mm. Between August 2020 and June 2024, the settlement spread to the northern and western sides, as well as the built-up areas of Bright Pearl Island. While the rate of spread gradually slowed, the cumulative settlement continued to increase, with the settlement degree along the western outer sea of Bright Pearl Island being the most pronounced, with the maximum cumulative settlement reaching 59.28 mm.

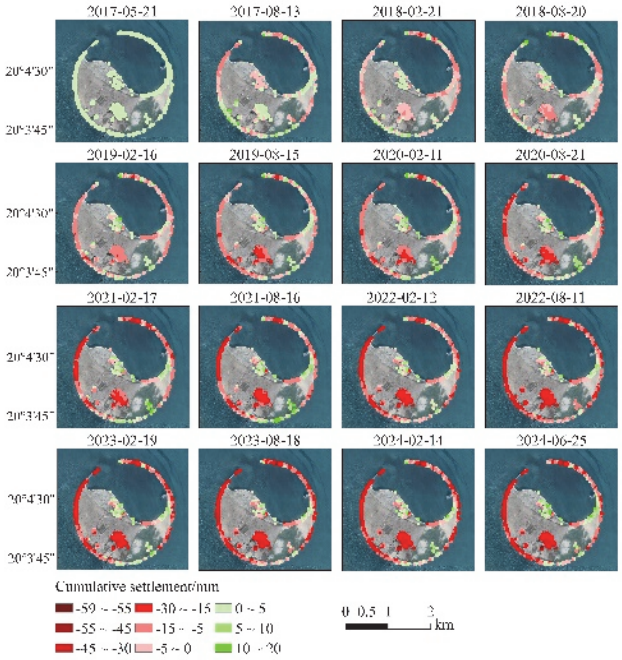


**Figure 11** Time-series cumulative surface settlement in Bright Pearl Island

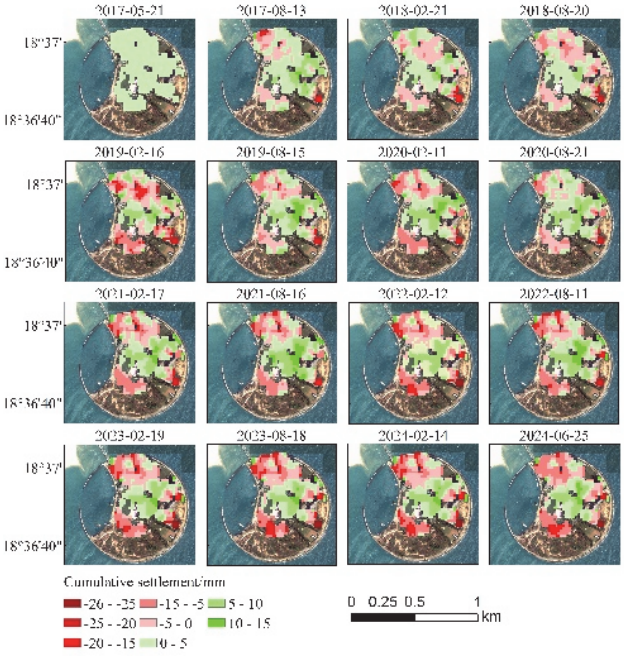


**Figure 12** Time-series cumulative surface settlement in Wanning Sun Island

As illustrated in Fig. 12, Wanning Sun Island remained largely stable throughout the monitoring period from 2017 to 2024, with cumulative settlement ranging from –5 to 5 mm. Settlement was primarily concentrated in the building areas located in the outer ring of the island center. From May 2017 to June 2024, the settlement rate in the above-mentioned areas was slow, but the cumulative settlement continued to increase. The maximum settlement occurred in a hotel along the eastern side of Wanning Sun Island facing the outer sea, where the maximum cumulative settlement reached 25.48 mm. Overall, the settlement rate of Wanning Sun Island is slower, compared to Ocean Flower Island and Bright Pearl Island, and the most affected areas of Wanning Sun Island show less than half the settlement seen on the other two islands.

To explore the time - series evolution of land settlement on artificial islands, 12 feature points, selected from areas with significant land settlement to examine their deformation from May 2017 to June 2024, were analyzed. Fig. 4a shows the specific locations of 6 feature points on Ocean Flower Island. P1 is the stabilization and control point within Island 1#, while P2, P3, and P4 are settlement points along the outer sea on Islands 3#, 1#, and 2#, respectively. P5 and P6 are located in the central construction areas of Islands 3# and 2#. As shown in Fig. 13a, P1's cumulative settlement is within 20 mm. The remaining five feature points exhibit varying rates of nonlinear settlement. P2, P3, and P4 experienced rapid settlement followed by slower settlement from August 2017 to February 2022, with significant fluctuations. From February 2022 to November 2023, the settlement rate increased again, exceeding the previous period in both rate and duration. Between November 2023 and June 2024, settlement entered a fluctuating and decreasing state, with maximum settlements of 41.85 mm, 33.61 mm, and 42.75 mm, respectively. P5 and P6 underwent rapid settlement from August 2017 to August 2018, with settlements of 20.76 mm and 17.01 mm, respectively. From August 2018 to February 2022, settlement slowed. From February 2022 to November 2023, settlement increased rapidly again. Between November 2023 and June 2024, settlement entered a fluctuating state, with maximum settlements of 37.69 mm and 48.79 mm, respectively. The average maximum cumulative settlement of these five feature points is more than twice that of P1.

The locations of three feature points on Bright Pearl Island are shown in Fig. 4b. P7 acts as the stabilization control point on the island, while P8 and P9 are settlement points along the outer sea to the west and north, respectively. As can be seen from Fig. 13b, P7 is relatively stable compared to P8 and P9 in terms of settlement, with more noticeable settlement occurring between October and December each year. The settlement rates of P8 and P9 along the outer coastline increase over time, with the settlement being more stable during other periods. From May 2017 to May 2019, P7, P8, and P9 experienced rapid settlement, with settlement amounts reaching 15.52 mm, 16.24 mm, and 22.7 mm, respectively. From May 2019 to November 2021, P7, P8, and P9 settled more slowly, with settlement amounts reaching 25.36 mm, 25.99 mm, and 34.07 mm, respectively. From November 2021 to June 2024, P7, P8, and P9 settled steadily, with the maximum cumulative settlements reaching 37.68 mm, 35.7 mm, and 42.16 mm, respectively. These three feature points display non-linear settlement at different rates. The land settlement process initially saw rapid settlement after reclamation, followed by a gradual reduction in the settlement rate, which eventually stabilized.

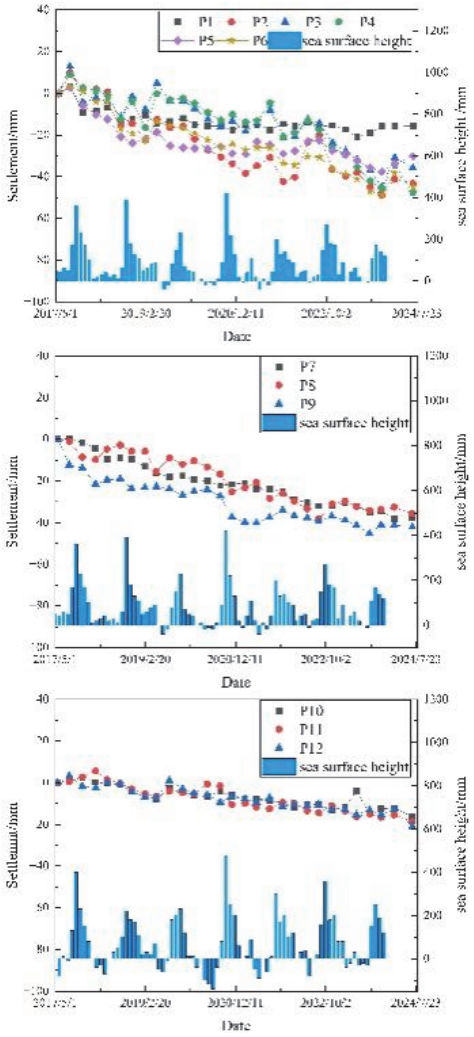


**Figure 13** Relationship between cumulative settlement and sea surface height at the characteristic points. (a) Ocean Flower Island; (b) Bright Pearl Island; (c) Wanning Sun Island

The locations of three feature points on Wanning Sun Island are shown in Fig. 4c. P10 is located at the settlement point beneath the center of Wanning Sun Island, while P11 and P12 are positioned at settlement points on the northern and eastern sides of the island. As depicted in Fig. 13c, P10-P12 are experiencing slow settlement, with their cumulative settlement not exceeding 21 mm. From May 2017 to May 2019, P10, P11, and P12 were in a stage of slowed settlement, with settlement amounts reaching 9.36 mm, 5.71 mm, and 8.31 mm, respectively. From May 2019 to June 2024, P10, P11, and P12 were in a stage of stable settlement, with the maximum settlement amounts reaching 16.3 mm, 18.65 mm, and 21.01 mm, respectively. These three feature points display similar nonlinear settlement rates, with minor fluctuations. The temporal evolution of settlement shows an initial phase of uplift, followed by a decline, with the settlement rate gradually slowing down and eventually stabilizing. In general, compared to Ocean Flower Island and Bright Pearl Island, the settlement on Wanning Sun Island is more stable.

### 4.2 Analysis of land Settlement Patterns on Artificial Islands

To examine the settlement patterns of the artificial islands following reclamation and to analyze their historical land reclamation, historical images from Google Satellite and Xinzhi Satellite Map were used. The reclamation of 3# Island, 2# Island, and the B area of 1# Island on Ocean Flower Island was completed in 2017 [21]. As illustrated in Fig. 14b, Bright Pearl Island's reclamation was also finalized in 2017. The changes in land settlement on these islands closely correspond with the monitoring period. Figs. 13a and b show that the settlement of points P2-P6 and P7-P9 occurred in three phases: rapid settlement, decelerating settlement, and stabilization [21]. Fig. 14a reveals that the reclamation of Island 1# of Ocean Flower Island was finished in 2015. After two years of settlement, characteristic point P1 from block E of Island 1# was selected. As depicted in Fig. 13a, P1 was already in the decelerating settlement phase by 2017, exhibiting a relatively slow settlement rate. From 2017 to 2024, it progressed into the stable settlement phase. Wanning Sun Island completed its reclamation in 2013, and after four years of settlement, characteristic points P10-P12 of Wanning Sun Island, shown in Fig. 13c, had entered the later stages of slowed settlement by 2017, with a notably slow rate. Between 2017 and 2024, P10, P11, and P12 gradually transitioned into the stable settlement phase. The temporal evolution of land settlement on the artificial islands follows three distinct phases: rapid settlement, slowed settlement, and stabilization [22]. This pattern is characterized by initially high settlement rates that significantly decrease, with the rate gradually slowing and ultimately stabilizing, as noted in previous studies. This trend also accounts for the stable settlement performance of Wanning Sun Island compared to Ocean Flower Island and Bright Pearl Island during the monitoring period from 2017 to 2024.

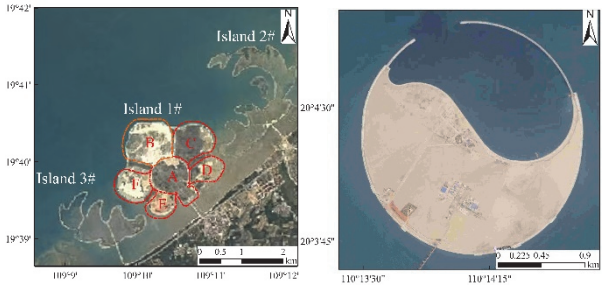


**Figure 14** The initial stage of artificial island construction. (a) 2015-12-31 Ocean Flower Island New Satellite Images; (b) 2017-3-13 Bright Pearl Island Google Earth Images

### 4.3 Correlation between Land Settlement and Ocean Hydrodynamics on Artificial Islands

The hydrodynamic conditions in Yangpu Bay are characterized by strong tidal forces and relatively weak wave action. As illustrated in Fig. 10, the settlement process occurs in distinct stages. Initially, settlement is concentrated within the island, but it gradually extends outward over time. Once the settlement of the entire island begins to stabilize, the settlement in the outer sea continues to increase [21]. By June 24, 2024, the total settlement at observation points in the outer sea of Ocean Flower Island reached 30.85 mm, while the inner sea area generally remained below 10 mm. Fig. 13a shows that the characteristic points P2, P3, and P4 along the outer sea of Ocean Flower Island exhibit significant fluctuations in settlement. Additionally, points P5 and P6, located near the outer sea at a moderate distance, experienced notable fluctuations due to construction activities between August 2017 and August 2018. Since August 2018, the fluctuations have been further intensified by settlement in the outer sea, although they are less pronounced than those at P2, P3, and P4. In contrast, point P1 in the inner sea saw rapid settlement from May to November 2017, after which the rate of settlement gradually decreased, and fluctuations became much smaller. These findings suggest that the outer sea areas are subject to stronger marine hydrodynamic forces compared to the inner areas [23]. The settlement along the outer coastline of Ocean Flower Island is significantly greater than that of the inner area, indicating spatial variability in the settlement deformation of the calcareous sand artificial island, as noted in previous research [24].

The tidal currents in the Qiongzhou Strait are quite strong, and Bright Pearl Island, located within this strait, experiences considerable marine hydrodynamic effects [17]. These conditions may have impacted the land settlement of the artificial island, indicating a need for further research. The time-series settlement data presented in Fig. 11 shows that settlement along the outer sea of Bright Pearl Island has increased over time. By June 24, 2024, the cumulative settlement at the observation points around the island's outer sea averaged approximately 20.25 mm. The western section of the island saw the most pronounced settlement, averaging about 28.12 mm, with a maximum of 59.28 mm. Additionally, Fig. 13b demonstrates that the settlement at points P8 and P9 along the outer sea is more significant and varies greatly, while P7, situated in the inner sea, has shown a consistent decline with minimal variation. The variability in land deformation on Ocean Flower Island and Bright Pearl Island tends to rise as one moves closer to the outer sea.

Previous research has indicated that rising sea levels accelerate land deformation rates [25]. To investigate the relationship between land deformation trends and sea level changes, the monthly average sea level variations along the western and eastern coasts of Hainan Province from 2017 to 2023 were analyzed, as reported in the China Sea Level Bulletin by the Ministry of Natural Resources. Ocean Flower Island and Bright Pearl Island are situated in western Hainan, while Wanning Sun Island is located in the east. The findings, illustrated in Fig. 13, show that rising sea levels generally lead to increased groundwater levels in coastal areas, which can enhance soil saturation, particularly in highly permeable blown-sand and silty soils. The rising groundwater table can compress these soils, especially those that are not fully consolidated, resulting in settlement in the unconsolidated blown-sand and silty soils. As shown in Figs. 13a and 13b, changes in sea level elevation are closely associated with land deformation, with the most significant settlement occurring when sea levels peak, typically between October and December when the water table is highest. As sea levels rise, cumulative settlement decreases rapidly. For instance,

from August to November 2017, the sea level around Ocean Flower Island increased from 60 mm to 360 mm, while the average cumulative settlement at P2, P3, and P4 fell from 8.02 mm to -5.91 mm. Similarly, from August to November 2020, the sea level around Bright Pearl Island rose from 20 mm to 410 mm, and the average cumulative settlement at P8 and P9 along the outer sea decreased from −22.2 mm to −32.6 mm. This trend has been consistent each year, indicating a strong link between land deformation and sea level changes. The results imply that land deformation on Ocean Flower Island and Bright Pearl Island is affected by the relative elevation of sea level.

As shown in Fig.12, the settlement on Wanning Sun Island is more stable than on Ocean Flower Island and Bright Pearl Island. Fig. 13c illustrates that the settlements at the characteristic points P10, P11, and P12, located on the island, show minimal fluctuation and remain relatively stable. The field survey reveals that riprap has been used along the coastlines of Ocean Flower Island and Bright Pearl Island. These riprap structures are mainly designed to mitigate the impact of waves and protect the shoreline. However, as shown in Fig. 15, the outer sea area of Wanning Sun Island is surrounded by caissons and vertical wave walls. Compared to riprap, which dissipates wave energy through irregular gaps and porous surfaces, the vertical retaining walls provide a continuous and rigid barrier that reflects wave energy more effectively, minimizing infiltration and erosion. These structures effectively reduce the impact of marine hydrodynamic forces and lessen the wave impact on the island's interior. Additionally, the deeper foundational embedding of vertical walls enhances resistance to scouring, offering long-term stability that surpasses the gradual displacement common in loose riprap systems. This situation indicates that the marine hydrodynamic environment and the relative height of the sea level also affect the artificial islands and are constrained by the construction methods. Therefore, it can explain why the settlement along the coast of Wanning Sun Island is much more stable compared to the other two islands.

**Figure 15** Along Wanning Sun Island (a) Tank along Wanning Sun Island; (b) Vertical retaining wall along Wanning Sun Island

### 4.4 Land Settlement on Artificial Islands and the Effects of Construction and Human Activities

As shown in Figs. 16a and 16b, construction activities on Islands 3# and 2# of Ocean Flower Island saw significant growth from December 2017 to March 2018, in contrast to Island 1#. Fig. 10 displays the locations of settlement observation points on Ocean Flower Island, revealing that most settlement areas are located within the construction zones, with a strong correlation between the spatial distribution of settlement and these areas. Notably, rapid settlement occurred in the construction zones of Islands 3# and 2#, accompanied by temporary uplift in the surrounding areas [26]. Over time, the effects of settlement from Islands 3# and 2# extended outward from the construction center, with the settlement area continuing to grow until it reached a considerable level by August 2018. The initial uplift followed by swift settlement near the construction zones is likely due to the lateral movement of silty soil under load, resulting in temporary uplift, which is then followed by rapid settlement as the soil adjusts or consolidates. To quantitatively assess the impact of construction on land settlement, the percentage of observation points within the construction zones was determined by identifying points with settlement values below –10 mm from the time-series InSAR data. This analysis revealed that 72.8% of the observation points were situated in or near the construction zones, highlighting the effect of ongoing construction activities. The settlements at key points P5 and P6 increased significantly from December 2017 to August 2018, with cumulative settlements for P1, P5, and P6 rising from 8.23 mm, 5.19 mm, and 0.16 mm to 13.74 mm, 20.76 mm, and 17.01 mm, respectively. This suggests that the E area of Island 1#, where P1 is located, was developed two years earlier, resulting in relatively stable settlement compared to P5 and P6.

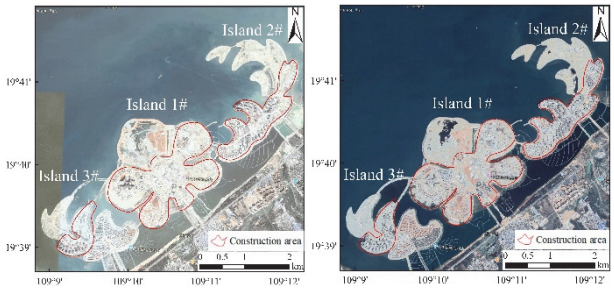


**Figure 16** The evolution of the ground construction space of Ocean Flower Island No.3. (a) 2017-12-27 Google Earth Images; (b) 2018-03-10Google Earth Images

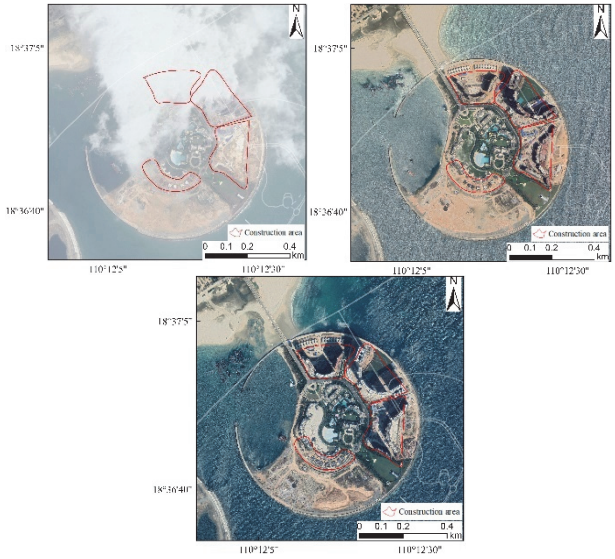


**Figure 17** The evolution of the ground construction space of Wanning Sun Island. (a) 2017-10-14 Google Earth Images; (b) 2018-04-01 Google Earth Images; (c) 2019-02-07 Google Earth Images

As can be seen from Fig. 17, from October 2017 to February 2019, it was found that the buildings extending outward from the center of Wanning Sun Island were under

construction. In conjunction with the settlement distribution shown in Fig. 12, settlement points on Wanning Sun Island with total settlements less than −2 mm were identified. Affected by the continuous construction, 86.9% of the observation points were located in the construction area. It is evident that the land settlement on the artificial island is mainly concentrated in the construction areas and is significantly influenced by engineering disturbances [24]. This indicates that the construction on the artificial island controls the spatial distribution of land settlement.

To examine the effects of human activities on land deformation, Fig. 10 illustrates that following the opening of Ocean Flower Island to tourists in February 2022, settlement levels in most areas of the island increased. The time-series settlement curve analysis in Fig. 13a indicates a notable acceleration in settlement. Five key points (P2, P3, P4, P5, and P6) experienced rapid settlement, while P1's settlement was comparatively slow. Between February 2022 and November 2023, P1's settlement rose from 14.64 mm to 17.35 mm, whereas the average settlement for points P2 to P5 surged from 18.69 mm to 45.11 mm, with P3 showing the most significant increase from 8.07 mm to 45.61 mm. This suggests that the E area of Island 1# of Ocean Flower Island, where P1 is situated, was constructed two years before the monitoring began, resulting in relatively stable settlement compared to other points. In contrast to the 2017-2018 period, the settlement rates for P2, P3, P4, P5, and P6 have accelerated, a trend that has persisted for over 18 months. Fig. 12 shows that after Wanning Sun Island opened to the public in October 2018, the settlement area expanded. In SAR analysis results revealed that in August 2018, 41.2% of settlement observation points recorded more than 2 mm of settlement, which increased to 56.8% by May 2019, indicating a significant rise in settlement area. As depicted in Fig. 13c, the average cumulative settlement for points P10-P12 rose from 0.56 mm to 7.28 mm between August 2018 and May 2019, reflecting an accelerated settlement rate. Conversely, Bright Pearl Island, which has not yet opened to the public, shows minimal settlement fluctuations at points P8 and P9, aside from sea level influences. Point P7, unaffected by construction, sea level changes, or human activities, exhibits a relatively stable natural settlement trend. This underscores that human activities significantly impact the settlement of artificial islands, aligning with previous research findings [27].

## 5 CONCLUSIONS

This study evaluates the effectiveness of InSAR technology for monitoring ground settlement on artificial islands. By analyzing multi-scene ascending track Sentinel-1A remote sensing images of Hainan Island, we identified the land deformation patterns of various artificial islands in the region and examined the spatial and temporal changes in settlement, along with the factors affecting it. The main findings are as follows:

1. Between May 2017 and June 2024, the average annual settlement rates for Ocean Flower Island, Bright Pearl Island, and Wanning Sun Island were −1.95 mm/a, −2.09 mm/a, and −0.41 mm/a, respectively. On Ocean Flower Island, settlement was primarily observed in the outer sea area, with the highest cumulative settlement of 88.01 mm occurring near Island 2. Bright Pearl Island experienced most of its settlement on the northern and western sides, with a maximum cumulative settlement of 59.28 mm on the west side. In contrast, Wanning Sun Island exhibited slower and more stable settlement, with a maximum cumulative settlement of 25.48 mm. The temporal evolution of land deformation on these artificial islands follows a three-phase pattern post-construction: rapid settlement, slowed settlement, and stabilization.

2. Ocean Flower Island and Bright Pearl Island are significantly influenced by the marine hydrodynamic environment, with increased settlement rates observed closer to the outer sea. The land deformation on these islands is affected by the relative sea level height. Wanning Sun Island, however, is protected by caissons and vertical retaining walls, which reduce the impact of external ocean currents. This suggests that the effects of the marine hydrodynamic environment and sea level height on artificial islands are also dependent on the construction techniques used.

3. The spatial distribution of land deformation on artificial islands is closely linked to construction activities. On Ocean Flower Island, settlement spreads outward from construction sites, indicating a pattern of development from the island's center to its periphery. In contrast, land deformation on Wanning Sun Island is mainly concentrated in the construction zones. Additionally, human activities can intensify the settlement process on these artificial islands.

## Acknowledgments

This work was supported by the National Natural Science Foundation of China (No. 52178282); National Key Research and Development Program (No. 2022YFD2401302); Commissioned project (No. MW-KYHT-2024002).

## 6 REFERENCES

[1] Li, S., Wang, N., Zhang, L., & Song, N. (2013). Ecological impacts of marine reclamation in Bohai sea from 1981 to 2011. *Marine Enviromental Science*, *32*, 926-929+938.

[2] Wu, Q., Jia, C. T., Chen, S. B., & Li, H. Q. (2019). SBAS-InSAR Based Deformation Detection of Urban Land, Created from Mega-Scale Mountain Excavating and Valley Filling in the Loess Plateau: The Case Study of Yan'an City. *Remote Sensing*, *11*(14), 1673. https://doi.org/10.3390/rs11141673

[3] Xu, Q., Dong, X., & Li, W. (2019). Integrated Space Air-Ground Early Detection, Monitoring and Warning System for Potential Catastrophie Geohazards. *Geomatics and Information Science of Wuhan University*, *44*(07), 957-966. https://doi.org/10.13203/j.whugis20190088

[4] Xu, Q. (2020). Understanding and Consideration of Related Issues in Early Identification of Potential Geohazards. *Geomatics and Information Science of Wuhan University*, *45*(11), 1651-1659. https://doi.org/10.13203/j.whugis20200043

[5] Zhu, J., Li, Z., & Hu, J. (2017). Research Progress and Methods of InSAR for Deformation Monitoring. *Acta Geodaetica et Cartographica Sinica*, *46*(10), 1717-1733. https://doi.org/10.11947/.AGCS.2017.20170350

[6] Liu, X., Shang, A., Jia, Y., & Wei, C.(2016).Application Contrast of PS-InSAR and SBAS-InSARin Urban Surface

settlement Monitoring. *GNSS World of China*, *41*(02), 101-105.

[7] Ferretti, A., Prati, C., & Rocca, F. (2000). Nonlinear settlement rate estimation using permanent scatterers in differential SAR Interferometry. *IEEE Transactions on Geoscience and Remote Sensing*, *38*(5), 2202-2212. https://doi.org/10.1109/36.868878

[8] Berardino, P., Fornaro, G., Lanari, R., & Sansosti, E. (2002). A New Algorithm for Surface Deformation Monitoring Based on Small Baseline Differential SAR Interferograms. *IEEE Transactions on Geoscience & Remote Sensing*, *40*(10), 2375-2383. https://doi.org/10.1109/TGRS.2002.803792

[9] Xu, Q., Pu, C., Zhao, K., He, P., Zhang, H., & Liu, J. (2021). Time Series InSAR Monitoring and Analysis of Spatiotemporal Evolution Characteristics of Land settlement in Yan'an New District. *Geomatics and Information Science of Wuhan University*, *46*(07), 957-969. https://doi.org/10.13203/j.whugis20200146

[10] Cavalié, O., Sladen, A., & Kelner, M. (2015). Detailed quantification of delta settlement, compaction and interaction with man-made structures: the case of the NCA airport, France.*Natural Hazards and Earth System Sciences Discussions*, *3*(6), 3761-3788. https://doi.org/10.5194/nhess-15-1973-2015

[11] Jiang, L. & Lin, H. (2010). Integrated analysis of SAR interferometric and geological data for investigating long-term reclamation settlement of Chek Lap Kok Airport, Hong Kong. *Engineering Geology*, *110*(3-4), 77-92. https://doi.org/10.1016/j.enggeo.2009.11.005

[12] Zeng, M., Pi, P., Zhao, X., Chen, S., Peng, H., Hou, Q., Sun, H., & Xue, Z. (2023). Spa-tial-temporal Characteristics of Land settlement in the Typical Reclamation area of PearlRiver Estuary Based on PS-InSAR. South China Geology. *South China Geology*, *39*(1), 116-126.

[13] Nie, Y., Xiong, Q., Ji, Y., & Wang, B. (2023). Monitoring Surface settlement in Nanhui New City Reclamation Based on SBAS-InSAR Technology. *Urban Geotechnical Investigation & Surveying*, *3*(1), 71-75.

[14] Fang, P., Wang, J., & Wang, D. (2018). The medium and long term settlement of reclamation airports. *Protective Engineering*, *40*(4), 70-78.

[15] Zhang, S., Ma, J., Li, H., Deng, J., & Li, Z. (2023). Research on reinforcement techniques for soft coral sand foundations. *Protective Engineering, 45*(6), 71-78.

[16] Nie, S. (2016). *Study on deep foundation pit deformation rule and numerical simulation of the "1# huahai island entertainment center*. Master's Thesis, Hubei University of Technology, Wuhan, China.

[17] Shi, P., Cao, L., Mo, W., & Xie, J. (2015). Influence of man-made island construction on the stability of the beach in the west coast of Haikou Bay. *Journal of Tropical Oceanography*, *34*(4), 57-63. https://doi.org/10.11978/2014124

[18] Zhang, D., Shi, L., Gong, Z., & Guo, J. (2022). Evolution characteristics of beach erosion and accretion at the Riyue Bay under the combined impacts of winter waves and artificial island. *Journal of Tropical Oceanography*, *41*(4), 71-81. https://doi.org/10.11978/2021150

[19] Chen, B., Gong, H., Li, X., Lei, K., Duan, G., & Jie, J. (2014). Spatial-Temporal Evolution Characterization of Land settlementDwMulti-Temporal InSAR Method and GIS Technology. *Spectroscopy and Spectral Analysis*, *34*(4), 1017-1025. https://doi.org/10.3964/j.issn.1000-0593(2014)04-1017-09

[20] Qu, F., Zhang, Q., Lu, Z., Zhao, C., Yang, C., & Zhang, J. (2014). Land settlement and ground fissures in Xi'an, China 2005-2012 revealed by multi-band InSAR time-series analysis. *Remote Sensing of Environment*, *155*, 366-376. https://doi.org/10.1016/j.rse.2014.09.008

[21] Ge, M., Li, N., Zhang, W., Zheng, J., & Zhu, C. (2017). Settlement behavior and inverse prediction of post-construction settlement of high filled loess embankment. *Chinese Journal ofRock Mechanics and Engineering*, *36*(3), 745-753. https://doi.org/10.13722/j.cnki.jrme.2016.0014

[22] Zhong, X. (2017). *Morphodynamics of the beaches around Hainan Island: The normal processes, the influences of extreme events and artificial island construction*. Doctoral Dissertation, East China Normal University, Shanghai, China.

[23] Zhang, Z,. Zuo, S., & Cui, C. (2018). Numerical Simulation Study on the Embankment Project of the EnclosedSea and Its Influence in Haihua Artificial Islands in Hainan. *Water Conservancy Science and Technology and Economy*, *24*(2), 16-22. https://doi.org/10.3969/j.issn.1006-7175.2018.02.004

[24] Lan, H., Zhao, X., Wu, Y., Li, L., & Su, F. (2017).Settlement and Deformation Characteristics of Calcareous lsland- reef. *Periodical of Ocean University of China, 47*(10), 1-8. https://doi.org/10.16441/j.cnki.hdxb.20160483

[25] Sheng, H., Wu, M., Chen, Y., Luo, M., & Zhuang, X. (2017). Superposition Analysis of Land settlement and Sea Level Rise. *Preventing Geological Disasters and Removing Risks for Peaceful Living - 2017 Annual Academic Conference of Zhejiang Geological Society*, *2017*, 596-599.

[26] Gong, X., Xu, Q., Pu, C., Chen, W., Xiu, D., & Ji, X. (2024). InSAR Time Series Monitoring and Analysis of Land Deformation after Mountain Excavation and City Construction in Lanzhou New Area. *Geomatics and Information Science of Wuhan University*, *49*(2), 236-245. https://doi.org/10.13203/j.whugis20210553

[27] Zhou, L., Guo, J., Hu, J., Li, J., Xu, Y., Pan, Y., & Shi, M. (2017). Wuhan Surface settlement Analysis in 2015-2016 Based on Sentinel-1A Data by SBAS-InSAR. *Remote Sensing*, *9*(10), 982-982. https://doi.org/10.3390/rs9100982

**Contact information:**

**Shusu DUAN**
(Corresponding author)
School of Civil and Architectural Engineering, Hainan University,
Haikou Hainan, 570228, China
E-mail: 993040@hainanu.edu.cn

**Haixiang HUANG**
School of Civil and Architectural Engineering, Hainan University,
Haikou Hainan, 570228, China

**Zhi ZHOU**
School of Civil and Architectural Engineering, Hainan University,
Haikou Hainan, 570228, China

**XueXin YANG**
Hainan Provincial Highway Administration, Danzhou Highway Bureau,
Danzhou Hainan, 571170, China

**Xin YANG**
Hainan Provincial Water Conservancy and Hydropower Group co., Ltd.,
Haikou Hainan, 570203, China

**Weihua WANG**
Hainan Provincial Water Conservancy and Hydropower Group co., Ltd.,
Haikou Hainan, 570203, China

**Xiaoxiang CHEN**
Hainan Provincial Water Conservancy and Hydropower Group co., Ltd.,
Haikou Hainan, 570203, China